DARK MATTER AND BARYON FRACTION AT THE VIRIAL RADIUS IN ABELL 2256

MAXIM MARKEVITCH[1] AND ALEXEY VIKHLININ[1]
Harvard-Smithsonian Center for Astrophysics, 60 Garden Street, Cambridge, MA 02138;
maxim@head-cfa.harvard.edu, alexey@head-cfa.harvard.edu

ABSTRACT

We combine high-quality *ASCA* and *ROSAT* X-ray data to constrain the radial dark matter distribution in the primary cluster of Abell 2256, free from the assumption of gas isothermality. Both instruments indicate that the temperature declines with radius. The region including the central galaxy has a multicomponent spectrum, which results in a wide range of allowed central gas temperatures. We find that the secondary subcluster has a temperature and luminosity typical of a rich cluster; however, the *ASCA* temperature map shows no signs of an advanced merger in this double system. It is therefore assumed that the primary cluster is in hydrostatic equilibrium. The data then require dark matter density profiles steeper than $\rho \propto r^{-2.5}$ in the cluster outer part. Acceptable models have a total mass within $r = 1.5 \ h^{-1}$ Mpc (approximately the virial radius) of $6.0 \pm 1.5 \times 10^{14} \ h^{-1} \ M_\odot$ at the 90% confidence level. This is about 1.6 times smaller than the mass derived assuming isothermality. The gas fraction is correspondingly higher and is $0.08 \pm 0.02 \ h^{-3/2}$. A lower limit on the fraction of gas in the total local density at the same radius is $0.09 \ h^{-3/2}$, which is twice the isothermal value. Near the center, dark matter profiles with and without central cusps are consistent with the data. Our inferred total mass inside the X-ray core ($r = 0.26 \ h^{-1}$ Mpc) is $1.28 \pm 0.08 \times 10^{14} \ h^{-1} \ M_\odot$, which exceeds the isothermal value by a factor of 1.4. Although the confidence intervals above may be underestimates, since they do not include uncertainties arising from asymmetry and departures from hydrostatic equilibrium, the behavior of the mass distribution, if applicable to other clusters, can bring X-ray and lensing mass estimates into better agreement but aggravate the "baryon catastrophe." The observed considerable increase in the gas content with radius, not anticipated by simulations, may imply that a significant fraction of thermal gas energy comes from sources other than gravity and merger shocks, such as supernovae-driven galactic winds, for example.

Subject headings: dark matter — galaxies: clusters: individual (A2256) — intergalactic medium — X-rays: galaxies

1. INTRODUCTION

It has long been suggested that measuring the density and temperature distributions of the intergalactic gas would allow a cluster mass determination free from the limitations inherent in the virial estimates based on galactic velocities (Bahcall & Sarazin 1977; Mathews 1978). The necessary requirement that the gas be in hydrostatic equilibrium in the cluster gravitational well is largely met in most regular clusters (e.g., Sarazin 1988; Navarro, Frenk, & White 1995; see § 4.2). The gas density profile for symmetric clusters can readily be obtained with an imaging instrument, such as *Einstein* or *ROSAT*. Obtaining temperature distributions has proven to be more problematic. In the absence of spatially resolved spectral data, much work has been done assuming constant temperature.

At small cluster radii and outside of the central cooling flow regions, this assumption indeed applies (e.g., Watt et al. 1992; Ikebe et al. 1996; Loewenstein & Mushotzky 1996a). However, mass estimates at large radii are only as good as the temperature measurements at those radii. This is illustrated by large uncertainties of the inferred mass when allowance for nonisothermality is made (e.g., Henry, Briel, & Nulsen 1993, hereafter HBN, obtain a 68% range spanning a factor of 3 for the A2256 mass within $r_{\rm vir}$; see also Loewenstein 1994). Cosmological simulations predict that cluster gas temperatures decline at large radii (e.g., Tsai, Katz, & Bertschinger 1994; Navarro et al. 1995; Evrard, Metzler, & Navarro 1996). At the time of this writing,

however, only Coma and A2163 have temperature measurements at radial distances exceeding $1 \ h^{-1}$ Mpc.

The *Advanced Satellite for Cosmology and Astrophysics* (*ASCA*; Tanaka, Inoue, & Holt 1994) is capable of measuring the cluster temperature spatial distributions. It does indeed observe a significant temperature decline at large off-center distances in a number of hot, massive systems, such as A2163 (Markevitch et al. 1996, hereafter M96a), A2256, A2319, A665 (Markevitch 1996, hereafter M96), A2218 (Loewenstein 1997), and, probably, in the cooler A3558 (Markevitch & Vikhlinin 1997, hereafter MV) and Hydra A (Ikebe et al. 1997). Earlier *EXOSAT* and *Ginga* data on Coma (Hughes, Gorenstein, & Fabricant 1988; Hughes 1991) and Spacelab 2 results on Perseus (Eyles et al. 1991) suggested qualitatively similar temperature behavior. Henriksen & White (1996) infer a radial temperature decline for several clusters from comparison of spectra obtained with *HEAO 1* and *Einstein* SSS with different fields of view. If declining temperature profiles are typical (as is indeed suggested by our *ASCA* work in progress), it would imply that there is in fact less dark matter in cluster outskirts and probably more in the inner parts, compared to the results derived under the isothermal assumption. In this paper we will quantify this effect for A2256 and discuss some of its implications.

A2256 ($z = 0.058$) is among those clusters with a detected temperature decline. Although it may not be the best candidate for a convincing mass measurement, due to the presence of substructure (see § 4.1), the quality of the available X-ray data for this cluster is unsurpassed. There are six deep

---

[1] Also Space Research Institute, Russian Academy of Sciences.

ROSAT PSPC pointings covering different cluster regions out to $r \simeq 3 \ h^{-1}$ Mpc (Briel et al. 1991, hereafter B91) and a high–statistical quality *ASCA* temperature map for $r < 1$ h^{-1} Mpc with useful spatial resolution (M96). A2256 is therefore a good starting point for a mass determination using a measured temperature profile. A similar earlier effort on the more distant A2163 (M96a) has suggested that the dark matter density in that cluster falls off rather steeply with radius—but it has also suggested that A2163 may be out of hydrostatic equilibrium at the radii of interest. More evidence has since been added by Squires et al. (1997) that A2163 indeed is an advanced merger. Below, essentially the same method as that used in M96a is applied to A2256, which is better resolved and more likely to be in hydrostatic equilibrium. We parameterize $H_0 \equiv 100 \ h$ km s^{-1} Mpc^{-1}; all quoted errors are 90% one-parameter intervals.

2. *ROSAT* DATA

B91 have shown that A2256 is a double X-ray cluster. In addition, one of the X-ray brightness peaks coincides with the brightest cluster galaxy and is displaced by about $1\overset{'}{.}7$ from the primary cluster's centroid. To derive the density profile of the primary cluster, we have fitted the *ROSAT* PSPC image by two symmetric projected β-models (eq. [3] below; e.g., Jones & Forman 1984) representing the two subclusters, their a_X, β, center positions, relative normalizations, and the X-ray background being free parameters, plus a Gaussian brightness peak at the position of the central galaxy (fixing $\sigma = 1'$, as suggested by the HRI image). *ROSAT* PSPC data are analyzed as described in MV. For image analysis only energies 0.7–2 keV were used to optimize statistics, and the *ROSAT* point-spread function (PSF) model was taken from Hasinger et al. (1993). The best-fit centroid coordinates, luminosities, and gas distribution parameters for the components of the fit are summarized in Table 1.

For the primary cluster, we obtain $a_X = 5\overset{'}{.}64 = 0.259 \ h^{-1}$ Mpc and $\beta = 0.816$ for the emission measure profile (confidence contours are shown in Fig. 1), taking into account the small effect of the observed temperature decline (M96; § 3) and excluding the detectable point sources. These parameters are derived using the data from $r < 25'$ for self-consistent use in the *ASCA* analysis below. The corresponding central electron density (excluding the central galaxy) is $n_{e0} = 3.1 \pm 0.1 \times 10^{-3} \ h^{1/2}$ cm^{-3}. Our simplifying assumption that the central galaxy is projected rather than embedded in the primary cluster introduces a small inaccuracy of the central density distribution of the main cluster. However, this inaccuracy is insignificant compared to the uncertainty in the central temperature that will be obtained below; we discuss this issue further in § 5.1.
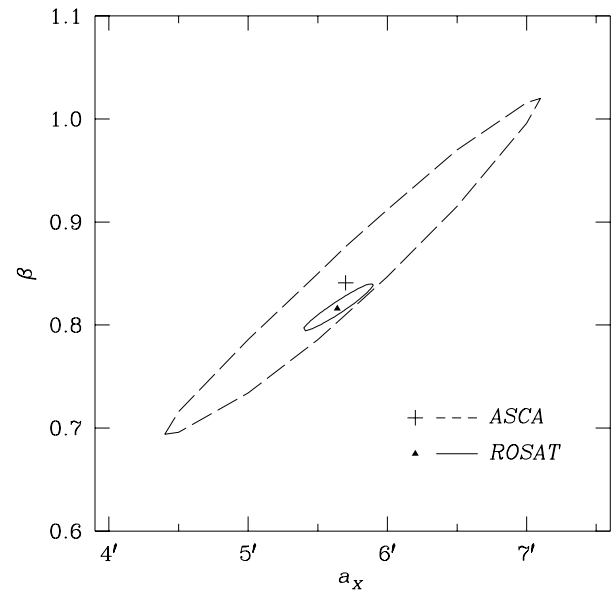

FIG. 1.—Two-parameter 90% confidence regions on a_X and β of the primary cluster gas density profile from *ASCA* and *ROSAT*. For *ASCA*, all temperatures and the spectrum of the central source were free parameters. For both instruments, parameters a_X and β of the secondary cluster were fixed at their best-fit values; the *ROSAT* fit excluded the region of the central source.

Regarding the adequacy of the β-model at large radii, the primary cluster emission can still be traced at the $1 \ \sigma$ level, including the background uncertainty, out to $r = 60'$, which is twice the virial radius (the radius inside which the cluster mean density is 180 times the closure density, $r_{\rm vir} \simeq 1.5 \ h^{-1}$ Mpc for A2256, using our mass measurement). Using data within $r = 60'$ we obtain $a_X = 5\overset{'}{.}51$ and $\beta = 0.801$, which are not significantly different from the above values. This is contrary to the simulation predictions of steepening gas profiles with radius (e.g., Navarro et al. 1995; see, however, Frenk et al. 1996). Fixing a_X and using only the profile in the several smaller intervals of radii, we find that the global value of β represents the local density slope to about $\pm 5\%$ accuracy in the inner cluster part. At the radii where the background uncertainty dominates, the possible error is greater: for $r = 20'-40'$, we obtain $\beta = 0.83 \pm 0.17$. These uncertainties will be included in the mass estimates discussed below.

For the smaller subcluster, $a_X = 3\overset{'}{.}9 \pm 0\overset{'}{.}4$ and $\beta = 0.92 \pm 0.12$. These parameters are poorly constrained, but they are not important for our final results; thus, in the following analysis they are fixed at their best-fit values. The two subclusters' 0.5–2 keV luminosities within $r = 1 \ h^{-1}$ Mpc are given in Table 1. The smaller subcluster is 2 times

TABLE 1
PARAMETERS OF IMAGE COMPONENTS FROM *ROSAT* PSPC

COMPONENT	CENTROID POSITION (J2000)		$L_X h^2$ (0.5–2 keV) (ergs s^{-1})	DENSITY PROFILE	
	R.A.	Decl.		a_X arcmin	β
Primary cluster......	$17^{\rm h}04^{\rm m}35\overset{\rm s}{.}8$	$78°36'54''$	8.9×10^{43}	5.64	0.816
Subcluster............	17 03 11.0	78 39 40	4.3×10^{43}	3.9	0.92
Central source[a]......	17 04 29.0	78 38 35	0.45×10^{43}	...	...

NOTE.—Units of right ascension are hours, minutes, and seconds, and units of declination are degrees, arcminutes, and arcseconds.

[a] Coordinates are fixed at the optical position of the brightest galaxy; Gaussian brightness profile width is fixed at $\sigma = 1'$.
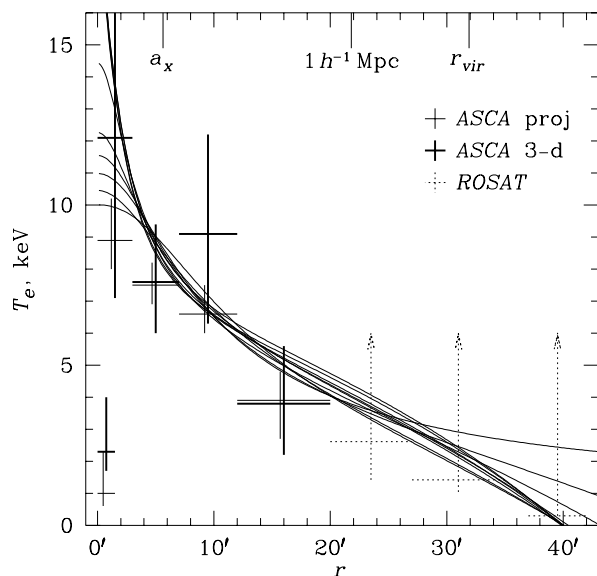
FIG. 2.—Temperature profile of the primary cluster. *ASCA* values correspond to steplike profiles in projected annuli or spherical shells (upper axis gives conversion to linear distances), while *ROSAT* values are for projected annuli. The central low temperature shows an additional component required in the central region. Errors are 90%. The lower limit at $r = 40'$ reflects the *ROSAT* detection of the cluster emission there. Smooth lines show a representative set of models (not projected and not showing the cooler component) allowed at the 99% confidence level by the *ASCA* data and the *ROSAT* 40′ limit (see text).

less luminous than the primary cluster; this differs from the finding of B91 (one-fifth of the primary cluster's luminosity). The difference is due to the fact that B91 refer to an excess flux in the 90° image sector containing the subcluster, while we refer to the full flux in the subcluster's β-model. Fitting the PSPC spectrum of the subcluster while subtracting the emission of the primary component as do B91, fixing the value of $N_H = 5 \times 10^{20}$ cm^{-2}, and using the 0.5–2 keV band (as in MV), we obtain $T_e = 4.1$ (2.5–8.2) keV, consistent with the *ASCA* result given below.

The PSPC-measured profile of projected temperatures in the inner $r \simeq 1$ h^{-1} Mpc of A2256 agrees remarkably well with the *ASCA* radial temperature gradient (MV), but, due to its relatively large errors, it is not used in the mass analysis below. Figure 2 shows PSPC temperature measurements at still greater radii, $r \simeq 1$–1.6 h^{-1} Mpc (excluding the 90° sector with the smaller subcluster), obtained using the same procedure as in MV. Although poorly constrained (mostly because of the background uncertainty), they suggest that the gas temperature continues to fall with radius. While keeping this in mind, we will not use these data below. More important for our analysis is the fact that the gas emission is still detected with 90% confidence at $r = 40' \simeq 1.8$ h^{-1} Mpc. We will conservatively interpret this as a lower limit on the gas temperature ($T_e > 0$ at that large radius) and apply this limit to the hydrostatic temperature profiles in § 5.

3. *ASCA* DATA

Technical details of the *ASCA* analysis of A2256, including discussion of the systematics, are given in M96, who presented a two-dimensional map of projected gas temperatures in this cluster. The analysis technique used there and in this work, which efficiently takes into account the complex *ASCA* PSF (Takahashi et al. 1995), is described in

M96a. The cluster temperature map shows that except for a cooler subcluster, there is no significant asymmetry in the radial decline of the projected temperature. Here we reconstruct a three-dimensional, as well as projected, radial temperature profile of the primary cluster. In this section we make no assumptions regarding the underlying mass distribution to indicate the intrinsic data constraints, while in § 5 continuous hydrostatic profiles will be constrained by the data. As in § 2, we assume that the main cluster is spherically symmetric, and that the smaller subcluster and the central source are projected onto it. It is also assumed for simplicity that the subcluster is isothermal, since it only contributes about 20% of the flux in the image region that determines the temperature in our most important outer spherical bin (for the same reason, the uncertainty in its brightness distribution is unimportant). Under these assumptions we first fitted uniform temperatures in four spherical shells of the primary cluster with radii corresponding at the cluster's distance to $r = 0'$–3′, $r = 3'$–7′, $r = 7'$–12′, and $r = 12'$–20′. Together with these we also fitted a temperature of the subcluster and various models for the central source, allowing its normalization to be a free parameter. The image regions from which *ASCA* spectra are collected are annuli defined by the above radii excluding the 90° sector containing most of the subcluster, this sector, and an $r = 1.5$ circle around the central galaxy. GIS and SIS spectra from all regions are fitted simultaneously.

Due to the limited *ASCA* angular resolution it is difficult to constrain both the temperature and spatial brightness distributions with *ASCA* alone. We therefore take advantage of the *ROSAT* information on the relative brightness distribution. Because the resulting *ASCA* temperatures are sensitive to the assumed brightness distribution, one must ensure consistency between the two instruments on this issue and that the use of the *ROSAT* image does not introduce an error in the temperature measurement. For this we fix a_X, β of the subcluster, and the positions of the three model components at their *ROSAT* values, but free the temperatures, relative normalizations of the model components (i.e., the main cluster, the subcluster, and the central source), and a_X and β of the primary cluster, thus using almost no *ROSAT* information in the *ASCA* fit. Confidence contours for the latter two parameters are shown in Figure 1. *ROSAT*- and *ASCA*-derived brightness distributions are in perfect agreement, while the *ROSAT* accuracy is superior. Therefore, a_X and β can be fixed at their *ROSAT* values, which we do below.

Assuming that the central source has the same temperature as the surrounding gas yields a gas temperature of 7.2 ± 1.5 keV in the central $r = 3'$ spherical bin. This may misleadingly suggest that the cluster central part is largely isothermal. However, if that source is allowed to have a different spectrum, χ^2 is significantly reduced by 13–18 for one additional parameter, depending on the assumed model, for which we tried a second thermal component, a cooling flow or a power law. A power-law model (with the best-fit photon index -2.4 ± 0.3) is formally the best fit, and we chose to use this model in further analysis (being aware that the real spectrum is probably still more complex). All models result in allowing a higher ambient gas temperature. In fact, due to the limited *ASCA* angular resolution, we cannot precisely localize the source of this additional emission: it may, for example, be one or more of the several radio sources in the central region (Röttgering et

al. 1994). There are no bright point sources in the relevant region of the *ROSAT* HRI image, which argues in favor either of a thermal or of a nonthermal extended component. However, its exact origin is not important for our analysis; therefore, we assume that it is the central galaxy. This spectral complexity, combined with projection, results in a relatively large uncertainty in the central temperature of the main gas component, which will complicate an accurate measurement of the mass distribution in the central region.

The best-fit temperatures in the radial shells of the primary cluster, with other parameters treated as described above, are shown in Figure 2 as thick crosses. For this model $\chi^2_{min} = 461$ for 685 degrees of freedom, reflecting our conservatism in accounting for the instrumental uncertainties. For a consistency check and to show the intrinsic data constraints separated from the uncertainty of the deprojection, we performed a similar analysis assuming uniform temperatures within projected regions on the sky rather than in spherical shells (even though it has less physical meaning). These temperatures are also shown in Figure 2 as thin solid crosses. The projected and three-dimensional temperatures differ as expected, with uncertainties of the latter being greater, due to the deprojection. Note that the steplike profiles assumed above have little physical meaning (since the real distribution is continuous), which, together with the natural anticorrelation of the errors in the adjacent spherical bins of the deprojected profile, explains differences such as that in the third annulus in Figure 2. This is not important for our mass analysis in § 5.1, in which continuous temperature profiles will be compared directly to the data.

For the smaller subcluster we obtain $T_e = 5.3 \pm 0.5$ keV and a relative iron abundance $0.35^{+0.16}_{-0.11}$, exceeding with marginal significance the value for the primary cluster, $0.23^{+0.09}_{-0.07}$. The temperature and the luminosity of the subcluster agree very well with the L_X-T relation of David et al. (1993). The iron abundance in the outermost parts of the primary cluster is unconstrained; we assume it to be uniform and fix it at the best-fit value.

4. VALIDITY OF HYDROSTATIC EQUILIBRIUM ANALYSIS

4.1. *Substructure and Possible Merger*

Before using X-ray data to derive the distribution of dark matter in A2256 under the assumption of hydrostatic equilibrium, we should address the adequacy of this assumption. Fabrican, Kent, & Kurtz (1989), B91, and Davis & Mushotzky (1993) showed that A2256 contains substructure both in the optical and X-ray data. This cluster has a radio halo and head-tail radio sources (Röttgering et al. 1994) that may be related to a merger (although their relation is not unambiguously established). A merger would result in significant gas turbulence and in the inadequacy of our assumption of spherical symmetry.

However, there is a strong argument against an advanced merger: the absence of any significant asymmetries of the gas temperature (M96) expected in a collision of such massive clusters (e.g., Schindler & Müller 1993). The detection of hot spots by Briel & Henry (1994) was later not confirmed by reanalysis of their data using an updated *ROSAT* PSPC calibration (MV). The accuracy of the *ASCA* measurement in M96 was adequate for detecting a temperature pattern characteristic of a merger if it existed, and indeed, such a pattern was observed in several clusters,

including the obviously merging A754 (Henriksen & Markevitch 1996). The observed probable difference in iron abundances of the subclusters (§ 3) also argues against a late-stage merger, since the gas would mix if clusters had passed through each other. Another argument is the presence of a remarkably long and straight narrow-tail radio source near the cluster center (Röttgering et al. 1994). Its existence strongly suggests that there is no significant gas turbulence there.

We therefore assume that the merger has not proceeded far enough to disturb the bulk of the primary cluster's gas. Moreover, below it will be assumed that the two clusters are physically well separated along the line of sight, so that the gravitational effect of the subcluster on the primary cluster's gas can be neglected. Indeed, such a separation is suggested by the galaxy velocity data. Fabricant et al. (1989) and B91 noted that the cluster line-of-sight velocity distribution can be described by two components, correspondent to the two subunits, separated by about 2000 km s^{-1}. A simple calculation (as in, e.g., Henriksen & Jones 1996) shows that, assuming two clusters of comparable masses falling from rest at some large distance toward each other, a main cluster mass of $7 \times 10^{14} \ h^{-1} \ M_\odot$ as obtained below, and the observed projected distance between the cluster centers, this rather small relative velocity implies a separation of 2–3 h^{-1} Mpc.

4.2. *More General Issues*

In a similar analysis of A2163, M96a raised the possibility that plasma in the outer, low-density region may be out of electron-ion temperature equipartition in such a way that the measured T_e underestimates the thermodynamic temperature. In A2256 the temperature measurements correspond to smaller radii and higher densities. In the radial bin where *ASCA* detects a temperature drop, the timescale for reaching equipartition via collisions is $\sim 7 \times 10^8 \ h^{-1/2}$ yr, which is shorter than the time that has to have passed since the last merger for the cluster to become relaxed as we observe it. Actual temperature measurements beyond this radius will not be used (only a lower limit, $T_e > 0$). The temperature decline in A2256 is also less steep than that in A2163, where it implied convective instability. At the radii of the temperature decline in A2256, the temperatures correspond to a polytropic index of 1.50 (1.24–1.9). Therefore, the gas should be convectively stable on large scales.

There is a possibility that some of the gas in the outer regions of the cluster is confined by the local potential wells of small, infalling subunits rather than by that of the primary cluster. If that is the case, one would not expect the cluster to be azimuthally symmetric, while the *ROSAT* image shows it is rather smooth out to large radii, except for a small ellipticity.

At large cluster radii residual bulk motions of gas from past merger events and infall may become nonnegligible, which would mean that hydrostatic equilibrium may not be an adequate assumption. Simulations of Evrard et al. (1996) showed that the kinetic energy of these motions can be anywhere between 0% and 70% of the gas thermal energy at the cluster virial radius, with high values corresponding to clusters experiencing mergers. Given that the bulk of A2256 seems to have been undisturbed in the recent past, as we concluded above, we can assume that A2256 is relatively well virialized within our radius of interest. A significance of this effect on the mass estimates, as well as the uncertainty

arising from our assumption of spherical symmetry, can best be assessed through the hydrodynamic simulations. Several independent authors (e.g., Tsai et al. 1994; Schindler 1996; Evrard et al. 1996; Roettiger, Burns, & Loken 1996) applied the X-ray mass estimation algorithm, which assumes spherical symmetry and hydrostatic equilibrium, to the simulated clusters in various cosmological backgrounds. They find that when the actual temperature profile is used (as we do), such estimates are on average unbiased and have a rms scatter around the true mass of about 15% at the core and about 30% at the virial radius. These are conservative estimates of the scatter, because clusters with obvious mergers, which show the biggest mass errors, are included in them but would be excluded by the observers (recall that the primary cluster of A2256 is not a merger, as we concluded above). Bartelmann & Steinmetz (1996) find their simulated X-ray mass estimates to be systematically biased and attribute their disagreement with other authors to their assumption of more severe observational conditions, which are not relevant to our present work. The values above may therefore be regarded as conservative estimates of the systematic uncertainty of an individual cluster mass determined by the X-ray method. We will continue this discussion in § 6.1 in its application to our results.

5. MASS CALCULATION

5.1. Method

The X-ray data will now be used to constrain the mass profile of the primary cluster. Because the gas temperature profile is known much less accurately than the gas density profile, we chose to use the fitting method of Hughes (1989) and HBN, with some technical variations. Two functional forms for the dark matter radial profile will be considered, which together can approximate just about any physically meaningful symmetric distribution: one with a constant core,

$$\rho_d \propto \left(1 + \frac{r^2}{a_d^2}\right)^{-\alpha/2}, \quad (1)$$

and one with a central singularity (cusp) predicted by cluster simulations (e.g., Navarro et al. 1995),

$$\rho_d \propto \left(\frac{r}{a_d}\right)^{-\eta}\left(1 + \frac{r}{a_d}\right)^{\eta-\alpha}. \quad (2)$$

In both profiles the density in the outer part declines asymptotically as $\rho_d \propto r^{-\alpha}$. Navarro et al. (1997) found that simulations in different cosmologies produce a "universal" density profile for clusters in equilibrium; it is of the latter form, with $\eta = 1$ and $\alpha = 3$. The isothermal sphere model corresponds to $\alpha = 2$; profiles with $\alpha = 2$–4 are expected under different assumptions about the cluster formation (e.g., Syer & White 1997 and references therein; Kofman et al. 1996). For the gas, we use a β-model density profile (Cavaliere & Fusco-Femiano 1976),

$$\rho_g = \rho_{g0}\left(1 + \frac{r^2}{a_X^2}\right)^{-3\beta/2}, \quad (3)$$

with a_X and β derived in § 2. For simplicity, the relatively small (of the order of 1%; HBN) contribution of galaxies to the total mass is neglected. With the above functional forms for the major mass components, we solve the hydrostatic equilibrium equation (e.g., Sarazin 1988) analytically (see Appendix) to recover the radial gas temperature profile for

a given set of parameters α, η (if applicable), a_d, the dark matter normalization ρ_{d1}, and the temperature at zero radius T_0. The general behavior of the solutions is discussed in detail by, e.g., Hughes (1989), HBN, and Loewenstein (1994). For dark matter profiles of the cusp form (2) and a β-model gas density profile, the gas temperature profile at $r = 0$ is finite if $\eta < 2$ and has zero derivative if $\eta < 1$. In practice the insufficient spatial resolution of the temperature data does not allow us to constrain all three shape parameters of the profile (2) independently; thus, we chose to fix $\eta = 1$, as suggested by simulations. Temperature profiles rising to infinity outside the measurable region are not allowed in our analysis (which in practice does not affect our constraints), but we do allow them to fall to zero at a finite radius (outside $r = 40'$, where *ROSAT* certainly detects cluster emission), since hydrostatic equilibrium is not expected to hold far from the virial radius.

In this work we are interested in the shape of the dark matter density distribution. Therefore, for a given set of the shape parameters α and a_d, we fit ρ_{d1} and T_0 so that, after the projection and convolution with the telescope responses, the temperature profile minimizes *ASCA*'s χ^2. The spectra and the normalizations of the additional central galaxy source and the subcluster are treated as free parameters, in order to allow maximum freedom for the temperature profile of the main cluster. The gas associated with the central galaxy is not included in the hydrostatic equilibrium equation, although in reality the central galaxy atmosphere resides in the same gravitational potential and is in pressure equilibrium with the main cluster gas that is being modeled. In principle, its temperature can be modeled in a similar way and used to provide additional constraints on the mass distribution in the center. However, in the absence of better resolution data on whether the two gas phases cohabit in the same volume or one of them replaces the other, we chose a conservative treatment that does not additionally restrict the range of mass models and consists of completely freeing the normalization and the spectrum of the central galaxy component. This approach should not significantly affect the mass measurements outside the $r \simeq 2'$ central galaxy region.

The model is fitted directly to the *ASCA* data (not to the steplike temperature profiles shown in Fig. 2). Minimum χ^2 values for both functional forms of the dark matter profile are very similar. They are also similar to the value obtained for the steplike temperature distribution; thus, this value can be considered an "absolute" minimum of χ^2 with which to compare the models of different form. Those models for which $\chi^2 > \chi^2_{min} + 4.6$ are rejected with 90% confidence. A profile acceptable for *ASCA* is then checked against the requirement that the temperature be greater than zero at $r = 40'$ (a lower limit from the *ROSAT* flux detection) and, if not complying, rejected at 90% confidence. The actual *ROSAT* temperature estimates between $r = 20'$ and $r = 35'$ do not constrain profiles any better than this lower limit; thus, for simplicity, they are not used. However, these estimates reinforce the lower limit, even if, contrary to our assumption, hydrostatic equilibrium does not hold at these large radii.

5.2. Results

A narrow range of hydrostatic temperature profiles is allowed by both *ASCA* and *ROSAT* constraints. Representative examples of the temperature profiles corresponding

to the models acceptable within the approximate combined 99% confidence region, as described above, are shown in Figure 2 (note that the temperatures in the central $r \lesssim 1'-2'$ may have little physical meaning, due to our incomplete treatment of the central galaxy atmosphere, as discussed above). The corresponding dark matter density and total mass profiles are shown in Figure 3. Shallow mass distributions best describe the *ASCA* temperatures alone, but they predict a temperature drop to zero immediately beyond the *ASCA* field of view, contrary to the *ROSAT* data. The combined data exclude, at greater than 99% confidence, those dark matter profiles with a core of the form (1) for which $\alpha < 2.5$, and those of the form (2) for which $\alpha < 3$, for any

value of the scale parameter a_d (these constraints on α in fact correspond to similar nonparametric slopes of the profile over the measured region). Very steep dark matter profiles with $\alpha > 4$, which correspond to the outer cluster regions being dominated by gas, are not excluded by the data, although they lack physical motivation. Naturally, acceptable profiles with shallower outer slopes have smaller a_d. For the acceptable dark matter profiles with cores, $a_d/a_X \simeq 0.3-1$ (that is, dark matter is more centrally peaked than gas), and for profiles with cusps, $a_d/a_X \simeq 1-2$ for the values of $\alpha \leq 5$ that we considered. For a particular value of $a_d = a_X \simeq r_{\rm vir}/6$, the most acceptable outer slopes are $\alpha \simeq 4$ and 3 for the core and the cusp profile forms, respectively; thus,
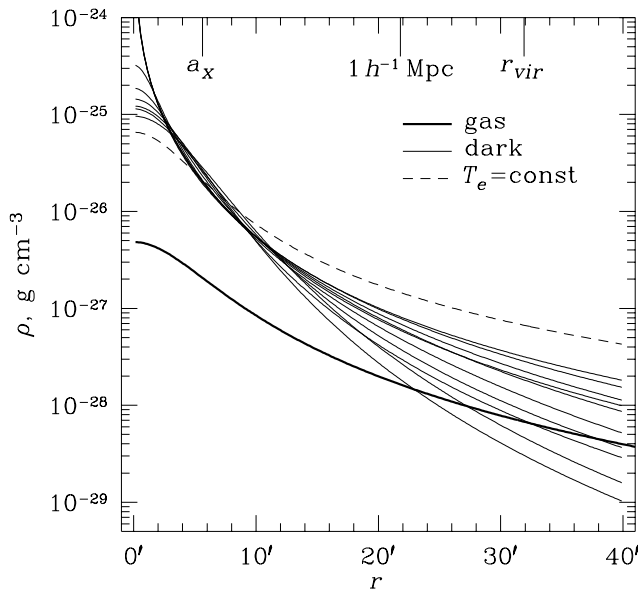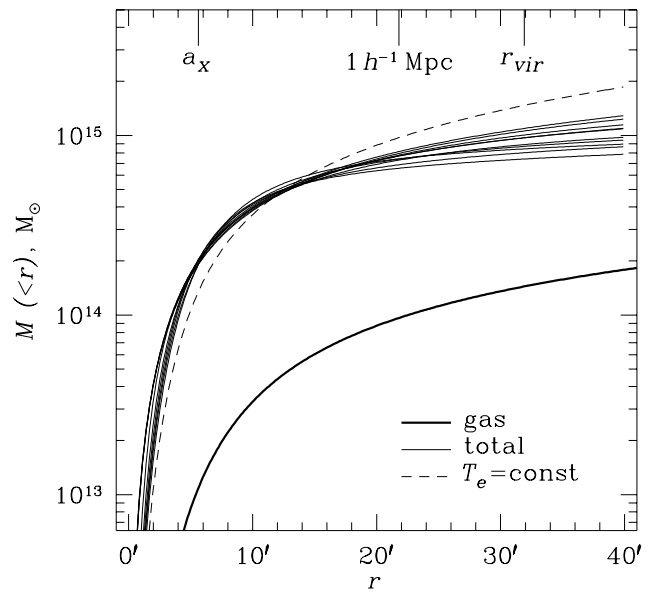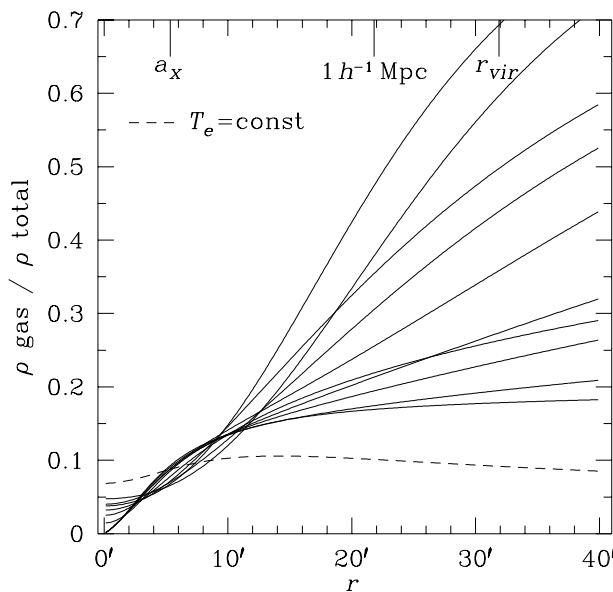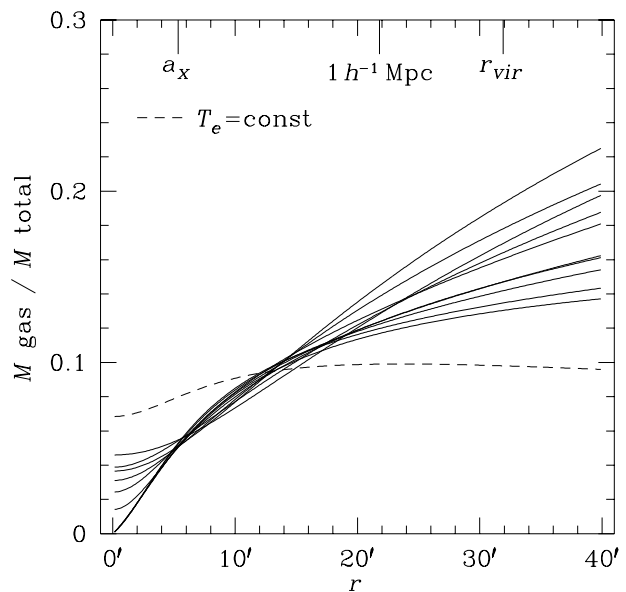

FIG. 3a

FIG. 3b

FIG. 3c

FIG. 3d

FIG. 3.—Models whose temperature profiles are shown in Fig. 2. (*a*) Their dark matter density profiles, (*b*) corresponding enclosed total masses (including gas), (*c*) fractions of the gas density in the total local density at a given radius, and (*d*) fractions of gas in the total mass within a given radius. Values from the isothermal analysis (for the cluster average $T_e = 7.5$ keV) are shown for reference. Acceptable profiles of both functional forms (with a core or a central $\rho_d \propto r^{-1}$ cusp) are shown for $\alpha \leq 5$. Absolute values are for $h = 0.65$ (total mass scales as h^{-1} and gas fraction as $h^{-3/2}$).

the "universal" profile of Navarro et al. (1997) appears to be acceptable.

At $r = 0.7 \; h^{-1}$ Mpc (about half the virial radius), where direct, accurate temperature measurements exist, the total mass for the allowed models is $3.8 \pm 0.3 \times 10^{14} \; h^{-1} \; M_\odot$ (for the mass values hereafter, we include in quadrature the uncertainties of the local gas density slope at the respective radii, as estimated in § 2). This mass is consistent with the value of $4.5 \pm 2 \times 10^{14} \; h^{-1} \; M_\odot$ obtained earlier by HBN at this radius (correcting for their distance error).

At the radius r_{500} (inside which the mean density is 500 times critical), which corresponds to $r = 0.92 \; h^{-1}$ Mpc for A2256, using our mass profile, the mass is $4.5 \pm 0.4 \times 10^{14} \; M_\odot$, which is significantly below the value of $7.2 \pm 1.9 \times 10^{14} \; M_\odot$ predicted by the scaling law of Evrard et al. (1996). This difference is due to the fact that the simulations typically produce a shallower temperature fall than the observed one. If the cluster had been isothermal, its mass within r_{500} would be $6.7 \times 10^{14} \; h^{-1} \; M_\odot$, in agreement with the scaling relation (in part because r_{500} itself would be slightly larger).

At $r = 1.5 \; h^{-1}$ Mpc (the virial radius), we obtain an unprecedentedly accurate estimate of the mass, $M = 6.0 \pm 1.5 \times 10^{14} \; h^{-1} \; M_\odot$. This value is significantly smaller, by a factor of 1.6, than the value obtained assuming isothermal gas, as is expected for a declining temperature profile and realistic matter distributions (e.g., Evrard et al. 1996). The local dark matter density is constrained less accurately, but it is possible to derive a strong upper limit beyond $r \sim 0.5 \; h^{-1}$ Mpc. This limit is 1.5–2 times lower than the isothermal value, although it is, of course, rather model dependent.

Because the central cluster temperature is poorly constrained, the density profile within the cluster X-ray core is as well—the profiles with and without a central density cusp are both acceptable. Nevertheless, the total mass internal to the core ($r = 0.26 \; h^{-1}$ Mpc) is well constrained as $1.28 \pm 0.08 \times 10^{14} \; h^{-1} \; M_\odot$ for the acceptable models. This is consistent with the Broad Band X-Ray Telescope measurement (restricted to $r < 0.4 \; h^{-1}$ Mpc; Miyaji et al. 1993) and is 1.4 times higher than the isothermal value.

6. DISCUSSION

6.1. *Accuracy of Mass Values*

The formal confidence intervals for the values given above represent only the experimental uncertainties (and as such are directly comparable to those from earlier works). Because of the high quality of the data, additional uncertainties of the method resulting from possible deviations from spherical symmetry and hydrostatic equilibrium, as predicted by simulations (§ 4.2), become comparable to or even exceed our experimental errors. We do not attempt to quantify these systematic uncertainties for A2256, since the main purpose of this paper is to compare the mass estimates obtained using the actual temperature profile with those from the isothermal analysis (to which the same systematic deviations apply). To draw reliable quantitative conclusions about the cluster mass profiles in general (which is our more distant goal), it is obviously necessary to study a sample of clusters, of which A2256 is the first member. Nevertheless, even for this individual cluster, the qualitative effects discussed below exceed the realistic uncertainties suggested by the simulations.

It is also noteworthy that the formal measurement accuracy is approaching a limit arising from the unknown cluster peculiar velocities and hence accurate distances d. The two components of A2256 have velocities differing by about 2000 km s^{-1}, and, thus, their distances calculated from redshifts may be in error by as much as 5%–7%, implying a similar error in mass within a given projected radius. In the absolute sense this uncertainty is small, and, of course, H_0 is not yet known to such accuracy. However, relative results may be significantly affected. For example, the observed difference of baryon fractions (which are proportional to $d^{3/2}$) between the low-z clusters A1060 and AWM7 (Loewenstein & Mushotzky 1996a) might be entirely explained if either of them had a peculiar velocity of 800–1000 km s^{-1}.

6.2. *Gas Fraction*

The mass value we obtain within $r_{\rm vir}$ corresponds to an average baryon fraction (which is higher than or equal to the gas fraction, $0.08 \pm 0.02 \; h^{-3/2}$) higher by a factor of 1.6 than the value obtained from the isothermal analysis. This change, if applicable to other clusters, would make the observed cluster baryon fraction even more contradictory to the hypothesis of $\Omega = 1$, as discussed, e.g., by White et al. (1993), White & Fabian (1995), and most recently by Evrard (1997). The gas fraction above formally implies that $\Omega \simeq 0.1$–0.25 for $h = 0.65$, if one assumes that the cluster matter content is representative of the universe as a whole, that dark matter is nonbaryonic, and the standard nucleosynthesis (Walker et al. 1991). Alternatively, assuming the high or low measured deuterium abundance (see, e.g., review in Steigman 1996), it implies that $\Omega \simeq 0.06$–0.13 and that $\Omega \simeq 0.2$–0.5, respectively.

As Figures 3c and 3d show, the gas fraction increases significantly with radius by about a factor of 2.5–3 from the radius of overdensity 10^4 ($r \sim a_X$) to $r_{\rm vir}$, even if one considers only the least steep models. Similar behavior is obtained for a sample of other clusters under the assumption of gas isothermality and for several cool systems taking into account the observed temperature gradients (David, Jones, & Forman 1995). Note that A2256 differs from clusters in that sample in its steeper gas density profile and in a considerably lower *isothermal* estimate of the gas fraction (which is also almost uniform with radius). However, the use of the actual temperature profile makes the value and the radial dependence of the gas fraction in A2256 rather similar to that of the rich clusters from David et al. (if the actual temperature profiles would not alter their results). As David et al. point out, differences in the distributions of gas and dark matter indicate that, in addition to gravity, reheating and hydrodynamics must play a role in the formation of structure on cluster scales. Loewenstein & Mushotzky (1996a) similarly interpret the observed difference (by a factor of ~ 1.5) of the individual baryon fractions in the central parts of A1060 and AWM7. Cluster simulations including shock heating of gas (e.g., Pearce, Thomas, & Couchman 1994; Navarro et al. 1995) plus radiative cooling (Frenk et al. 1996), but not including any additional sources of gas heating, indeed produce slightly antibiased gas profiles ($M_{\rm gas}/M_{\rm total} \propto r^{0.1}$ to $r^{0.2}$; Evrard 1997) because of the energy transfer from the dark matter and conversion of gas during galaxy formation. However, they do not produce the antibias of the observed degree, suggesting that some physics is still missing from the simulations. The most fre-

quently mentioned candidate is energy input from supernovae (see Sarazin 1988 for a review). Along a different line, e.g., David, Forman, & Jones (1991) and Loewenstein & Mushotzky (1996b) showed that the supernovae needed to reproduce the elemental abundances in clusters would also produce the amount of heat comparable to the gas thermal energy. Still, the published cluster simulations that attempt to model supernovae-driven galactic winds (e.g., Metzler & Evrard 1994) seem to fail to reproduce the observed difference between the gas and dark matter distributions.

6.3. *Shape of the Mass Profile and Lensing Masses*

At present our constraints on the mass profile can be directly compared only to another *ASCA* result, that for A2163 (M96a), since other work was limited by the unavailability of the temperature data at large radii. The constraints on A2163 were rather similar to those obtained here (total density profiles of the form [1] with $\alpha < 2.1$ were excluded, corresponding to a slightly stronger constraint on the dark matter slope), although they were less accurate, because of A2163's greater distance, and less conclusive, due to the merger in that system. Using an independent method based on the analysis of ellipticity of cluster X-ray images, Canizares & Buote (1997) infer that the density of dark matter in clusters falls off as $\rho_d \propto r^{-4}$ in the outer parts. This is very similar to what we find for A2256.

The shape of the dark matter halo may be an interesting cosmological probe (e.g., Hoffman & Shaham 1985; Crone, Evrard, & Richstone 1994; see, however, Navarro et al. 1997). Comparing a sample of just one cluster with the statistical conclusions of the simulations is uncertain and has to wait until more clusters are studied. It is interesting to note, in the meantime, that the shallow density profiles predicted by Kofman et al. (1996) for the CHDM universe are inconsistent with our A2256 results.

Gravitational lensing provides an independent measure of the cluster mass distribution (see review in Bartelmann & Narayan 1995). Often, masses inferred by this method are up to a factor of a few greater than those from X-rays in the central cluster regions (e.g., Loeb & Mao 1994; Wu 1994; Miralda-Escudé & Babul 1995; Tyson & Fischer 1995). In some (the most discrepant) cases, the lensing analysis is likely to overestimate the mass as a result of substructure (Bartelmann 1995) or projection (Daines et al. 1997). Bartelmann & Steinmetz (1996) showed that clusters selected for the presence of strong arcs are more likely to have substructure. However, with better temperature data, the X-ray mass estimates may also be revised upward, in better agreement with lensing measurements, as we find for A2256. Our inferred density profiles for both functional forms are more centrally peaked than the gas profile, in agreement with lensing results for other clusters (Bartelmann & Narayan 1995) and the A2163 finding (M96a). Note that profiles with high central densities would erroneously be excluded in our analysis, if one did not allow for the multicomponent spectrum in the central region (required by *ASCA*) and instead used a formally well-constrained single temperature artificially excluding the possibility of a hotter gas. This is similar to the result of Allen, Fabian, & Kneib (1996), who find that allowing for a multitemperature gas in the cooling flow region of PKS 0745 increases the X-ray–measured mass within the lensing radius by a large factor, such that the strong lensing and X-ray masses agree. There are no lensing data on A2256 for comparison, because it is too nearby. Ikebe et al. (1996, 1997) similarly note that central dark matter concentrations in the cD clusters Fornax and Hydra A are required, if the gas in their central regions is treated as multiphase, as required by the *ASCA* spectra.

The fact that the shallow dark matter distributions are excluded at large radii may also have implications for the weak-lensing mass estimates. These estimates at present are of a relative nature and require assumed model density profiles in order to obtain the absolute value of the mass in the central region. As Squires et al. (1996) note, the central mass inferred from their analysis of A2218 varies by a factor of 1.3, depending on the assumed density profile, with the steeper profiles resulting in lower values. Our results on A2256 prefer steep density profiles and hence favor the lower bound of the weak-lensing mass estimates.

Regarding the dark matter distribution near the center, we note that in a cluster whose gas has a constant density core and is supported only by its own pressure, a central dark matter cusp may be ruled out a priori, because it would require a convectively unstable central temperature peak. A2256 has a central density excess over the β-model, associated with the brightest galaxy, that we do not model adequately (for a given mass profile, it would reduce the hydrostatic central temperature), which is why this additional constraint was not applied here. For other clusters, this constraint can be used to devise an interesting test of the significance of nonthermal gas support (which was proposed as one explanation of the discrepant lensing and X-ray masses; Loeb & Mao 1994). If a relaxed cluster is found whose gas indeed follows a β-model all the way to the center, but whose lensing data nevertheless require a central density cusp, then the gas in the center must have nonthermal support.

7. SUMMARY

We constrained the mass distribution in the primary cluster of A2256, using actual gas temperature measurements at large radii derived from X-ray data of unsurpassed quality for any cluster to date. Our analysis has shown the following:

1. Dark matter density profiles steeper than $\rho_d \propto r^{-2.5}$ in the outer part are required by the data. Profiles with central cusps such as those predicted by simulations are consistent with the data. The mass is distributed rather differently from what may be inferred under the assumption of isothermal gas: the total mass internal to the cluster X-ray core is higher, while the mass within the virial radius is lower, both by factors of about 1.5, than the isothermal estimates.

2. If our results for A2256 are typical for other clusters, three particularly interesting implications would be that the X-ray and lensing masses converge, that the "baryon catastrophe" is even more pronounced than it is thought now, and that gravity and merger shocks are probably not the only significant source of heating of the cluster gas.

APPENDIX

SOLUTION OF THE HYDROSTATIC EQUILIBRIUM EQUATION

The hydrostatic equilibrium equation for a spherically symmetric cluster (e.g., Sarazin 1988),

$$\int_0^r 4\pi r^2(\rho_d + \rho_g)dr = 3.70 \times 10^{13} \, M_\odot \frac{T(r)}{1 \text{ keV}} \left(\frac{r}{1 \text{ Mpc}}\right) \frac{0.60}{\mu} \left(-\frac{d \ln \rho_g}{d \ln r} - \frac{d \ln T}{d \ln r}\right), \tag{A1}$$

can be rewritten as a differential equation for the gas temperature, assuming a gas density profile of the form (3):

$$\frac{dt}{dx} = \frac{3\beta x}{1 + x^2} t - \frac{A}{T_0} \frac{I(x)}{x^2}. \tag{A2}$$

Here we denote $x \equiv r/a_X$; $t \equiv T/T_0$, where T_0 is the gas temperature in keV at $r = 0$, so that $t(0) \equiv 1$;

$$A \equiv \frac{4\pi}{3.70 \times 10^{13}} \left(\frac{a_X}{1 \text{ Mpc}}\right)^2 \frac{\rho_{g0}}{1 \, M_\odot \text{ Mpc}^{-3}} \text{ keV}, \tag{A3}$$

and

$$I(x) \equiv \int_0^x y^2(1 + y^2)^{-3\beta/2}dy + \frac{\rho_{d1}}{\rho_{g0}} \int_0^x y^2 f_d(y)dy. \tag{A4}$$

The two integrals in the equation above correspond to the gas and the dark matter, respectively; $f_d \equiv \rho_d/\rho_{d1}$ (where ρ_{d1} is the dark matter density at the X-ray core radius a_X) denotes the dimensionless dark matter density, whose form is given by either equation (1) or equation (2). The integrals in equation (A4) can be worked out analytically for the density profiles we use, but it is faster to calculate them numerically directly than to evaluate the resulting special functions numerically.

Equation (A2) can be solved either numerically (as in, e.g., Hughes 1989) or analytically, as we do. The analytic solution is given by

$$t(x) = (1 + x^2)^{3\beta/2}\left[1 - \frac{A}{T_0} \int_0^x (1 + y^2)^{-3\beta/2} \frac{I(y)}{y^2} dy\right]. \tag{A5}$$

For a set of parameters a_d, α, η, ρ_{d1}, and T_0, we calculate the temperature profile using equation (A5). The parameters ρ_{d1} and T_0 are adjusted so that the profile approximates the *ASCA* data as described in § 5. In practice it is advantageous to fit the quantities ρ_{d1}/T_0 and T_0, rather than the above two, since in the limit of zero gas mass, the shape of the profile depends only on ρ_{d1}/T_0.

The scheme described here differs from the one used by Hughes (1989), HBN, and M96a in that we parameterize a dark matter profile rather than a total mass profile. This automatically excludes the unphysical solutions in which the dark matter density ($\rho_\text{total} - \rho_g$) is negative, which required the introduction of an additional H_0-dependent constraint.

REFERENCES

Allen, S. W., Fabian, A. C., & Kneib, J. P. 1996, MNRAS, 279, 615
Bahcall, J. N., & Sarazin, C. L. 1977, ApJ, 213, L99
Bartelmann, M. 1995, A&A, 299, 11
Bartelmann, M., & Narayan, R. 1995, in Dark Matter, ed. S. Holt & C. L. Bennett (New York: AIP), 307
Bartelmann, M., & Steinmetz, M. 1996, MNRAS, 283, 431
Briel, U. G., et al. 1991, A&A, 246, L10 (B91)
Briel, U. G., & Henry, J. P. 1994, Nature, 372, 439
Canizares, C. R., & Buote, D. A. 1997, in X-Ray Imaging and Spectroscopy of Cosmic Plasmas, ed. F. Makino (Tokyo: Universal Academy), 40
Cavaliere, A., & Fusco-Femiano, R. 1976, A&A, 49, 137
Crone, M. M., Evrard, A. E., & Richstone, D. O. 1994, ApJ, 434, 402
Daines, S. J., Jones, C., Forman, W., & Tyson, A. 1997, ApJ, in press
David, L., Forman, W., & Jones, C. 1991, ApJ, 380, 39
David, L., Jones, C., & Forman, W. 1995, ApJ, 445, 578
David, L., Slyz, A., Jones, C., Forman, W., Vrtilek, S. D., & Arnaud, K. A. 1993, ApJ, 412, 479
Davis, D. S., & Mushotzky, R. F. 1993, AJ, 105, 409
Evrard, A. E. 1997, MNRAS, in press
Evrard, A. E., Metzler, C. A., & Navarro, J. F. 1996, ApJ, 469, 494
Eyles, C. J., Watt, M. P., Bertram, D., Church, M. J., & Ponman, T. J. 1991, ApJ, 376, 23
Fabricant, D. G., Kent, S. M., & Kurtz, M. J. 1989, ApJ, 336, 77
Frenk, C. S., Evrard, A. E., White, S. D. M., & Summers, F. J. 1996, ApJ, 472, 460
Hasinger, G., Boese, G., Predehl, P., Turner, T., Yusaf, R., George, I., & Rohrbach, G. 1993, ROSAT Calibration Memo CAL/ROS/93-015
Henriksen, M., & Jones, C. 1996, ApJ, 465, 666
Henriksen, M., & Markevitch, M. 1996, ApJ, 466, L79
Henriksen, M. J., & White, R. E. 1996, ApJ, 465, 515
Henry, J. P., Briel, U. G., & Nulsen, P. E. J. 1993, A&A, 271, 413 (HBN)
Hoffman, Y., & Shaham, J. 1985, ApJ, 297, 16

Hughes, J. P. 1989, ApJ, 337, 21
———. 1991, in Clusters and Superclusters of Galaxies, ed. A. C. Fabian (Dordrecht: Kluwer), 54
Hughes, J. P., Gorenstein, P., & Fabricant, D. 1988, ApJ, 329, 82
Ikebe, Y., et al. 1996, Nature, 379, 427
———. 1997, ApJ, 481, 660
Jones, C., & Forman, W. 1984, ApJ, 276, 38
Kofman, L., Klypin, A., Pogosyan, D., & Henry, J. P. 1996, ApJ, 470, 102
Loeb, A., & Mao, S. 1994, ApJ, 435, L109
Loewenstein, M. 1994, ApJ, 431, 91
———. 1997, in X-Ray Imaging and Spectroscopy of Cosmic Plasmas, ed. F. Makino (Tokyo: Universal Academy), 67
Loewenstein, M., & Mushotzky, R. F. 1996a, ApJ, 471, L83
———. R. F. 1996b, ApJ, 466, 695
Markevitch, M. 1996, ApJ, 465, L1 (M96)
Markevitch, M., Mushotzky, R. F., Inoue, H., Yamashita, K., Furuzawa, A., & Tawara, Y. 1996, ApJ, 456, 437 (M96a)
Markevitch, M., & Vikhlinin, A. 1997, ApJ, 474, 84 (MV)
Mathews, W. G. 1978, ApJ, 219, 413
Metzler, C. A., & Evrard, A. E. 1994, ApJ, 437, 564
Miralda-Escudé, J., & Babul, A. 1995, ApJ, 449, 18
Miyaji, T., et al. 1993, ApJ, 419, 66
Navarro, J. F., Frenk, C. S., & White, S. D. M. 1995, MNRAS, 275, 270
———. 1997, ApJ, 490, 493
Pearce, F. R., Thomas, P. A., & Couchman, H. M. P. 1994, MNRAS, 268, 953
Roettiger, K., Burns, J. O., & Loken, C. 1996, ApJ, 473, 651
Röttgering, H., Snellen, I., Miley, G., de Jong, J. P., Hanisch, R. J., & Perley, R. 1994, ApJ, 436, 654
Sarazin, C. L. 1988, X-Ray Emission from Clusters of Galaxies (Cambridge: Cambridge Univ. Press)
Schindler, S. 1996, A&A, 305, 858

Schindler, S., & Müller, E. 1993, A&A, 272, 137
Squires, G., Kaiser, N., Babul, A., Fahlman, G., Woods, D., Neumann, D. M., & Böhringer, H. 1996, ApJ, 461, 572
Squires, G., Neumann, D. M., Kaiser, N., Arnaud, M., Babul, A., Böhringer, H., Fahlman, G., & Woods, D. 1997, ApJ, 482, 648
Steigman, G. 1996, Proc. IAGUSP Workshop on Young Galaxies and QSO Absorbers, ed. S. M. Viegas, R. Gruenwald, & R. R. de Carvalho, in press
Syer, D., & White, S. D. M. 1997, MNRAS, submitted
Takahashi, T., Markevitch, M., Fukazawa, Y., Ikebe, Y., Ishisaki, Y., Kikuchi, K., Makishima, K., & Tawara, Y. 1995, *ASCA* Newsletter 3 (NASA/GSFC)

Tanaka, Y., Inoue, H., & Holt, S. S. 1994, PASJ, 46, L37
Tsai, J. C., Katz, N., & Bertschinger, E. 1994, ApJ, 423, 553
Tyson, J. A., & Fischer, P. 1995, ApJ, 446, L55
Walker, T. P., Steigman, G., Kang, H.-S., Schramm, D. M., & Olive, K. A. 1991, ApJ, 376, 51
Watt, M. P., Ponman, T. J., Bertram, D., Eyles, C. J., Skinner, G. K., & Willmore, A. P. 1992, MNRAS, 258, 738
White, D. A., & Fabian, A. C. 1995, MNRAS, 273, 72
White, S. D. M., Navarro, J. F., Evrard, A. E., & Frenk, C. S. 1993, Nature, 366, 429
Wu, X.-P. 1994, ApJ, 436, L115